HHS Public Access

Author manuscript

Comput Med Imaging Graph. Author manuscript; available in PMC 2016 July 21.

Published in final edited form as:

Comput Med Imaging Graph. 2014 December ; 38(8): 803–814. doi:10.1016/j.compmedimag.2014.07.003.

An image processing approach to analyze morphological features of microscopic images of muscle fibers

Cesar Henrique Comin[a], **Xiaoyin Xu**[b], **Yaming Wang**[c], **Luciano da Fontoura Costa**[a], and **Zhong Yang**[d,*]

[a] University of Sao Paulo, Institute of Physics at Sao Carlos, Sao Paulo, Brazil

[b] Department of Radiology, Brigham and Women's Hospital, Harvard Medical School, Boston, MA, USA

[c] Department of Anesthesia, Brigham and Women's Hospital, Harvard Medical School, Boston, MA, USA

[d] Department of Clinical Hematology, Southwestern Hospital, The Third Military Medical University, Chongqing, China

Abstract

We present an image processing approach to automatically analyze duo-channel microscopic images of muscular fiber nuclei and cytoplasm. Nuclei and cytoplasm play a critical role in determining the health and functioning of muscular fibers as changes of nuclei and cytoplasm manifest in many diseases such as muscular dystrophy and hypertrophy. Quantitative evaluation of muscle fiber nuclei and cytoplasm thus is of great importance to researchers in musculoskeletal studies. The proposed computational approach consists of steps of image processing to segment and delineate cytoplasm and identify nuclei in two-channel images. Morphological operations like skeletonization is applied to extract the length of cytoplasm for quantification. We tested the approach on real images and found that it can achieve high accuracy, objectivity, and robustness.

Keywords

Cytoplasm; Nuclei; Skeletonization; Quantification; Segmentation; Muscle fiber

1. Introduction

Skeletal muscle is the most abundant tissue of the human body, occupying about half of the body weight in healthy adults [1]. Skeletal muscle is principally composed of individual muscle fibers (or muscle cells) that are arranged in a structured manner. Muscle fibers are formed in the development process from the fusion of myoblasts (primitive muscle cells that can potentially develop into a muscle fiber) in a process known as myogenesis. The long, cylindrical, multinucleated muscle fibers is the biggest cell in the body, generally of tens of

* Corresponding author. Tel.: +86 23 68752312. zyang@tmmu.edu.cn (Z. Yang).

Conflict of interest statement

The authors declare no conflict of interest.

micrometers in diameter and hundreds of micrometer in length. The cytoplasm of skeletal muscle fibers mainly consists of regularly arranged myofibrils, in which two components, actin and myosin filaments, are responsible for the striated appearance of skeletal muscles. Functionally, skeletal muscles not only control bodily movement through their contraction and relax but also constitute the largest metabolic pool of the body. Aberration of skeletal muscle is the cause of many muscular diseases, including cardiomyopathy [2–4], muscular hypertrophy [5,6], inflammatory muscle damage [7–9], muscle development [10,11], muscular dystrophies [12–14], amyotrophic lateral sclerosis (ALS) [15], and myasthenia gravis [16]. Many of these diseases have no effective treatment and some of them like muscular dystrophies have a high fatality rate [17,18].

In studying skeletal muscles there are multiple criteria in evaluating the healthy status of muscles, including functional improvement of muscles, biochemical changes in muscle mass, and morphology of muscle fibers observed under microscopes. In this paper we focus on developing an image processing approach to automatically analyze and quantify morphology of muscle fibers because many muscular diseases manifest themselves as abnormality in terms of changes in nuclei and cytoplasm of muscle fibers. For example, skeletal muscles are capable of undergoing hypertrophy (increase in their sizes) in response to increased loading, while it can become atrophy upon unloading or immobilization. Skeletal muscle fibers have been shown to gain newly formed nuclei via the fusion of myogenic cells with the adult fibers in muscular hypertrophy. In muscular atrophy, muscle fibers are shown to usually lose nuclei through apoptosis. As such, one important criterion in evaluating the efficacy of treatment under development is to assess whether normality in muscle fiber morphology can be restored, in combination with dynamic evaluation like muscle functions and *in vivo* imaging [19,20]. The large number of microscopic images of muscle fibers generated in a typical experiment can be on the order of hundreds, making it is time prohibitive and error prone for manual analysis. Computerized analysis can provide objective and quantitative measurements in a high-throughput manner and assist researchers to assess many direct features and derived characteristics of muscle fibers. For example, after finding nuclei and cytoplasm in images, computerized analysis can drive the nuclei-to-cytoplasm ratio of muscle fibers, a criterion widely used to assess the health of muscle fibers [21,22].

In this work we developed an image processing pipeline consisting of image segmentation, quantification, and morphological operations to analyze muscle fiber images in a high-throughput manner. We tested the method on muscle fiber images acquired from tissue samples stained for both nuclei and cytoplasm and found the method can achieve high objectivity and accuracy.

2. Materials and methods

2.1. Cell culture, immunostaining, and image acquisition

We harvested primary myoblasts from hind limb muscles of 4-week old C57BL/10 male mice as described in Rando et al. [23]. The myoblasts were expanded in Ham's F10 medium supplemented with 20% fetal calf serum and 5 ng/ml basic fibroblast growth factor on collagen-coated plates. After clone culture, the myoblasts were identified with anti-desmin

antibody through immunocytochemistry. To induce myogenic differentiation of the cultured myoblasts, the growth medium was replaced with differentiation medium (DMEM with 2% horse serum) after the percentage of coverage reached over 70%. For immunostaining, the differentiated cells were fixed with 4% paraformaldehyde for 30 min at 4 °C, washed and treated with 0.5% Triton-X 100 in PBS for 5 min at room temperature. Then the cells were incubated with primary antibody Myosin Heavy Chain (MHC) diluted in 1:50 (MEDCLA66, Accurate Chemical & Scientific Corp, NY) followed by incubation with a CyTm3-conjugated secondary antibody (Jackson Lab) diluted in 1:500 to observe the cytoplasm. The nuclei were counter-stained with 4,6-diamidino-2-phenylindole (DAPI). Pictures were taken using a laser microscope (Nikon Eclipse E600) and saved as TIFF images with a pixel size of 0.76 μm. Fig. 1 shows a typical image after merging the DAPI and MHC channels.

2.2. Image processing pipeline

As the original images were collected in two channels, one for cytoplasm and the other for nuclei, our image processing pipeline features two paths to analyze each channel separately. There are two challenges in extracting objects from this type of two-channel images. The first challenge is that the images may have an uneven background and objects have close adjacency among them. The second challenge is that due to limitations in staining and imaging, there are residual signals from the MHC channel in the DAPI channel and vice versa. For example, Fig. 2(a) shows the DAPI channel image of Fig. 1 and we can observe some weak components of cytoplasm in the image. Fig. 2(b) shows the MHC-stained cytoplasm of Fig. 1 and because nuclei are not stained by MHC, they appear as dark holes on the MHC channel image, which may affect the accuracy of segmenting cytoplasm if the dark holes are not taken into consideration.

From Fig. 1 we note that cytoplasm generally has an elongated ellipsoidal shape with varying lengths. We also note that cytoplasm tends to have an approximately straight profile, a fact that we will explore in our algorithm design to detect them. Our image processing pipeline is shown in Fig. 3, which consists of two paths, with one to process the cytoplasm channel and the other to process the nuclei channel. Each branch has two main steps, binarization and morphological analysis. At first, we give an overview of the image processing pipeline. In nuclei channel image processing we employed an adaptive thresholding method to binarize the images. The initial binarized result may consist of both individual and clustered nuclei and thus needs to be further processed. To segment clustered nuclei we calculated the distance transform of each object in the binarized image and apply a peak finding filter. We then determine the centroid of the peaks to account for flat peaks, obtaining the position and number of nuclei inside each object detected in the binarized image. In cytoplasm channel image processing, an adaptive threshold is used to segment the image. Then the segmentation result is merged with that from the nuclei channel image, which identifies the nuclei, to fill the small holes corresponding to the nuclei in the cytoplasm channel. By incorporating the results from the nuclei channel we avoid the necessity to identify small holes directly in the cytoplasm channel, a process that may generate false positives and false negatives. Then we perform skeletonization in the cytoplasm channel to extract the center lines of the cytoplasm. Last, we apply morphological analysis to separate adjacent cytoplasm and remove short spurs in the skeletons of

segmented cytoplasm and small areas in the cytoplasm images to clean up the results. Next we describe the steps in the image processing pipeline in more details.

2.2.1. Binarization—Binarization is performed on both channels of images to

1. Adaptively thresholding of the nuclei and cytoplasm channels separately. At this step, we employ a circular moving window W with a radius r to binarize each channel [24]. Specifically, for each pixel $p(x, y)$ in a (nuclei or cytoplasm) image we calculate the mean intensity $\bar{p}(x, y)$ of all pixels within W and calculate

$$\delta p(x,y) = p(x,y) - \bar{p}(x,y) \quad (1)$$

We then compare $\delta p(x, y)$ to a preset threshold T to classify $p(x, y)$ to 1 if $\delta p(x, y) \geq T$ or 0, otherwise. In our approach, we set T to 0.1 for the nuclei channel and 0.005 for the cytoplasm channel, while the radius of the circular window W was set to 20 pixels for both channels. After thresholding, we obtain the final binarized nuclei image, which we label $I_{nuclei}^{Binarized}$. The cytoplasm channel needs some additional processing, therefore we label the image obtained in this step as I_{cyto}^{Inter}.

2. We next perform a logical OR operation of the two binarized images $I_{nuclei}^{Binarized}$ and I_{cyto}^{Inter} to create a merged binarized image

$$I_{Merge} = I_{nuclei}^{Binarized} \cup I_{cyto}^{Inter} \quad (2)$$

where $\cup$ is the logical OR operation.

3. At this step we post-process I_{Merge} to remove artifacts. We applied an area filter of 300 pixels to identify small groups of pixels such that

$$I_{Artifact} = f\left(I_{Merge}\right) \quad (3)$$

where f is the area filtering process. Here a group of pixels is defined as pixels that are connected. Two pixels are considered connected if they are next to each other in the row or column direction of the image (i.e., diagonally adjacent pixels are not considered as connected in our case). The reason of identifying artifacts based on I_{Merge} instead of individual $I_{nuclei}^{Binarized}$ and I_{cyto}^{Inter} is to reduce the probability of incorrectly marking valid structure that may be partially binarized in both $I_{nuclei}^{Binarized}$ and I_{cyto}^{Inter}. If we apply the area filter on $I_{nuclei}^{Binarized}$ and I_{cyto}^{Inter} separately, this valid structure might be incorrectly identified as an artifact.

4. Based on $I_{Artifact}$ identified above we then remove artifacts from I_{Merge} to obtain

$$I_{cyto}^{Binarized} = I_{Merge} - I_{Artifact}. \quad (4)$$

5. In the process of binarization, small holes may be formed in the binarized cytoplasm image $I_{cyto}^{Binarized}$ due to the presence of nuclei or noise. At this step, we fill small holes less than 100 pixels in $I_{cyto}^{Binarized}$.

The nuclei channel segmentation result of Fig. 2(a) is shown in Fig. 4(a). The initial binarized result of the cytoplasm channel of Fig. 2(b) is shown in Fig. 4(b), from which we can observe that there are holes in the binarized cytoplasm results that are caused by the nuclei and small scattered areas. The result of filling the small holes is shown in Fig. 4(c) by incorporating the locations of nuclei from Fig. 4(a). Finally small scattered areas are removed to produce the binarized cytoplasm shown in Fig. 4(d). From the figure we note that while most cytoplasm is well segmented there is some cytoplasm connecting to others in the image. So at the next step we will employ morphological analysis to separate those cytoplasm.

2.2.2. Morphological analysis of the cytoplasm channel—At this step we apply morphological operations to segment $I_{cyto}^{Binarized}$ based on prior biological information. First, we modify the Palágyi algorithm to calculate the skeleton (or medial axis) of the binarized cytoplasm [25]. The skeleton corresponding to Fig. 4(d) is shown in Fig. 5(a). For better illustration we randomly chose three ROIs in Fig. 5(a) and show them in Fig. 5(b), (f), and (j). After finding the skeleton, we calculate the widths of all the cytoplasm by measuring the distance from the skeleton to the cytoplasm boundary. The corresponding results are shown in Fig. 5(c), (g), and (k), respectively. This step is implemented by measuring the Euclidean distance *d* from each point of the skeleton to the closest cytoplasm boundary point. The width of a cytoplasm is estimated as two times *d* along the skeleton. We also construct the network formed by the skeleton, which includes terminal nodes and bifurcation nodes that connects two or more branches. The constructed network is important for cytoplasm analysis as we need to separate individual cytoplasm that appears connected due to the limited image resolution. The constructed network is shown in Fig. 5(d), (h), and (l). In using the Palágyi algorithm short spiky branches may be created due to the noise in the image that affects the binarization process and such branches need to be removed. A short branch is considered noisy if its length is less than 10 pixels (or 7.6 μm), which is slightly larger than the average cytoplasm width. We chose this value because it is unlikely that a fiber has a length almost equal to its width, and therefore this value ensures that no real fibers are removed in this step. Fig. 5(e, i, and m) shows in green the small branches that are removed in this step. After obtaining the skeletons we proceed to separate touching or adjacent cytoplasms. Because we know *a priori* that cytoplasm does not make sharp turns, in other words, does not have a high curvature, we check each bifurcation point and compute the angles formed between the skeleton segments to determine which of them belong to the same cytoplasm and which one represents separate cytoplasm. Fig. 6 illustrates the process of computing

angles formed at bifurcation points and separating touching cytoplasms. At bifurcation point C, pairs of three line sections $\overline{AC}$, $\overline{BC}$, and $\overline{DC}$ form three respective angles, α, β, and γ. We then determine that line sections $\overline{AC}$ and $\overline{BC}$ constitute a valid cytoplasm object because β is close to 180° and α and γ are much less than 180°. In the case illustrated in Fig. 6, line sections $\overline{AC}$ and $\overline{BC}$ are determined to form the skeleton of one cytoplasm object while line section $\overline{DC}$ is considered as the skeleton of another cytoplasm object and it is then separated at the bifurcation point C. Since skeleton sections are not always straight lines, we perform a first-order line fitting to each skeleton segment near the bifurcation point. The lengths of the line sections used for fitting (i.e., the distance of points A, B and D to point C) may affect the accuracy of the result. On the one hand, if the lengths used are too small, the robustness of the angle calculation may be affected as noise in the skeleton near the bifurcation point may have a profound effect in determining the direction of each skeleton section. On the other hand, if the lengths used are too large, the skeleton sections may deviate too much from being a straight line and may also affect the accuracy of calculation. In this work, we set the length of each line section used in angle calculation to 10 pixels. Note that this length is large enough to avoid discretization effects in angle calculation. Next, we dilated the skeleton by several pixels to obtain an approximate representation of the original fibers. In Fig. 7(a) we show the overlap of the obtained skeleton on the original cytoplasm image. The dilated skeleton is shown in Fig. 7(b). Note that in the figure each fiber is represented by a different shade of gray.

2.2.3. Morphological analysis of the nuclei channel—The purpose of this step is to detect and segment the nuclei. In this work, we applied a distance transform on the binary nuclei image, $I_{nuclei}^{Binarized}$, in order to separate overlapping nuclei. First, we note that noise in the image acquisition process gives rise to very small connected components in the binarized image. Therefore, we need to remove such components while keeping valid nuclei that have small areas. The size of components caused by noise was found to be typically smaller than 30 pixels, while we found no nuclei having a size smaller than 60 pixels. Thus, we choose to remove all components smaller than 60 pixels. Note that this difference in size between the noisy components and the nuclei means that the results are weakly sensitive to this parameter. For example, modifying the threshold to 40 pixels changed the results by less than 0.1% for all measurements. In this step, we have a new image given by

$$I_{nuclei}^{Final} = I_{nuclei}^{Binarized} - f\left(I_{nuclei}^{Binarized}\right) \quad (5)$$

where f is, again, the area filtering process that identifies small components. We then apply a distance transform [26] on the resulting binary image. The distance transform works as follows. For each pixel that belongs to an identified object in I_{nuclei}^{Final}, we calculate the smallest distance between the pixel and the border of the object and assign the obtained value to the respective pixel in a new image $I_{nuclei}^{Distance}$. In Fig. 8 we show an binarized image (Fig. 8(a)) and the respective distance transform (Fig. 8(b)). The task of identifying individual nuclei is then converted into the task of finding peaks in the distance transform. For such a task we use a maximum filter with a circular mask of radius r_p pixels, that is, we

mark each pixel that has maximum intensity inside a disk of radius r_p centered at the pixel under consideration.

Note that r_p is an important parameter of the nuclei detection method as it sets the scale where we expect to find maximum values of the distance transform. In other words, the detected peaks will be separated by at least r_p pixels. Since our main objective is to separate peaks in the distance transform that are close to each other and belong to the same object (caused by overlapping nuclei), the chosen radius of the maximum filter is related to the minimum radius expected from a nucleus. As pointed out above, we found no nucleus with an area smaller than 60 pixels, which is equivalent to a minimum radius of roughly 4 pixels (supposing perfect circular nuclei), therefore we set $r_p = 4$ pixels (or equivalently, 3.04 μm). There are a few cases that a group of pixels have the same maximum value (i.e., a flat peak in the distance transform). In such cases we calculate the centroid of the flat region. We now have the positions of the nuclei in the nuclei channel, which can then be compared to the detected cytoplasm in the other channel to obtain geometric and morphologic measurements such as the number of nuclei in each fiber or number of nuclei per fiber length. We note that changing the radius of the peak finding filter does not change the positions of the detected nuclei as it only affect the total number of detected nuclei. The detected peaks from the nuclei shown in Fig. 8(a) can be seen in Fig. 8(c).

3. Results

To evaluate the performance of the image processing pipeline, we tested it on some muscle fiber images. To illustrate the effect of the whole pipeline, Fig. 9 shows the processing results of another sample image. A cytoplasm object in the center of Fig. 9(a) is transformed into a line, as shown in Fig. 9(b). This line is dilated to give an approximate representation of the fiber, as shown in Fig. 9(c). This result is combined with the corresponding binarized nuclei image (the original image is shown in Fig. 9(d)). The fiber in the center of Fig. 9(a) is extracted and shown in Fig. 9(e) with its nuclei. Since we also have the positions of the nuclei, we only need to find how many nuclei are in the region defined by this fiber, which is four in this case. Such quantitative results allow us to perform many types of analysis that are difficult to achieve in manual analysis. First, we can derive the number of nuclei per cytoplasm, which is a criterion used to measure the healthy status of cytoplasm and muscles. Fig. 10 shows the histograms of the number of nuclei per cytoplasm calculated over five tissue specimens acquired under one experimental condition. From the figure we can observe the specimens have similar distribution in terms of number of nuclei per cytoplasm. Similarly we can calculate the fiber lengths in a straight-forward manner. The fiber lengths of the five tissue samples are shown in Fig. 11 and their average and standard deviation is shown in the last picture of Fig. 11. In addition to fiber length we can easily measure the width of fibers and mean fiber width (Fig. 12). The deviation of fiber width is also shown in Fig. 13. Finally, we plot the number of nuclei versus the fiber length in Fig. 14. The scatter plots illustrate that the number of nuclei is positively correlated with the fiber length. For example, most fibers with two or fewer nuclei are less than 300 μm long. Fibers that have three nuclei may have a maximum length of 400 μm, as shown in samples 1–3. For fibers having more than six nuclei, their lengths are between 200 and 600 μm. To validate the performance of our method, we performed manual analysis on one sample image as the gold

standard as manual analysis is usually used by researchers to analyze muscle fiber images. The result of manual analysis is shown in Fig. S1 of the supplementary material. In Fig. 15 we show the comparison of the measurements obtained from manual analysis with the automated segmentation of the same sample. It is clear that the values are close, with no noticeable skewness or systematic bias. Therefore, we conclude that our method can accurately measure geometric and morphologic features of muscle fibers. Quantitatively, we can derive other morphological features and statistics from the images. Table 1 summarizes some features that the image processing pipeline measures, namely,

- Nuclei density: number of nuclei in an image divided by the image area.
- Fiber density: number of fiber in an image divided by the image area.
- Fraction of fiber area: the area occupied by all the fibers divided by the image area.
- Nuclei per fiber area: number of nuclei in an image divided by the total area of the cytoplasm.
- Total fiber length: the sum of all fiber lengths.

Supplementary Fig. S1 related to this article can be found, in the online version, at http://dx.doi.org/10.1016/j.compmedimag.2014.07.003.

The table also shows the measured values by manual analysis of sample number five. As for the computational speed of the method, in a desktop computer with an AMD Phenom II X4 955 processor and 200 MB memory, each image takes roughly 50 s to be processed using a Python script, as compared with the much longer time required in manual analysis.

4. Discussion

In this paper we presented an image processing pipeline to detect and segment nuclei and cytoplasm in microscopic images of skeletal muscle fibers. Skeletal muscle fibers are a special type of cells in the sense that they are multinucleated as each fiber consists of multiple fused cells. Together, the morphology of nuclei and cytoplasm play an important role in determining the health of muscle fibers where malformation of muscle fibers is the cause of many muscular disorders. Thus from a biomedical perspective it is critical to analyze both nuclei and cytoplasm in evaluating the health of skeletal muscle fibers. Microscopes provide a direct assessment of muscle fibers as we can separately stain nuclei and cytoplasm for imaging. Due to imperfect conditions in staining and imaging, the microscopic images however may have residual signals from the cytoplasm channel in the nuclei channel. The cytoplasm channel may have small holes in the images that are occupied by the nuclei. Therefore, processing each channel of images separately may not generate satisfactory results. The novelty of the method is that it segments nuclei and cytoplasm in a joint manner to utilize the locations of nuclei in one channel as an additional input to accurately segment cytoplasm in the other channel. Compared with manual analysis, the proposed method produces objective and quantitative results that can be saved for detailed statistical analysis. The image processing pipeline is highly automatic to process multiple

data sets. As such, the proposed method can be used to assist biologists and clinicians in muscle fiber image processing and analysis.

Supplementary Material

Refer to Web version on PubMed Central for supplementary material.

Acknowledgments

The work of C. H. Comin was supported by FAPESP grant 2011/22639-8. The work of X. Xu was supported by National Science Foundation award 0958345. The work of Y. Wang was supported by National Institutes of Health K02AR051181. The work of L. da F. Costa was supported by FAPESP grant 11/50761-2 and the CNPQ grant 573583/2008-0. The work of Z. Yang was supported by National Natural Science Foundation of China award 31171148.

Biography

Cesar Henrique Comin is pursuing his Ph.D. at University of Sao Paulo, Institute of Physics at Sao Carlos, Sao Paulo, Brazil. His research interests are in network analysis, image processing, and bioinformatics.

Xiaoyin Xu received his B.S. in industrial technology from the University of Wisconsin–Stout in 1993 and his M.S. and Ph.D. in Electrical and Computer Engineering from the Northeastern University (Boston, MA) in 1998 and 2002, respectively. He is currently a faculty member at the Department of Radiology, Brigham and Women's Hospital, Harvard Medical School (Boston, MA). His research interests are in biomedical imaging and bioinformatics.

Yaming Wang received her Ph.D. in biology from the Sichuan University in China. Her research interests are in cell therapy in muscular disorder treatment and bioinformatics.

Luciano da Fontoura Costa is a professor at University of Sao Paulo, Institute of Physics at Sao Carlos, Sao Paulo, Brazil. His research interests are in network analysis, image processing, and bioinformatics.

Zhong Yang received his Ph.D. in histology and embryology from the Third Military Medical University, Chongqing, China in 2000. From February 2007 to May 2010, he worked as a postdoctoral fellow at the Brigham and Women's Hospital, Harvard Medical School, in Boston, MA, USA, focusing on the plasticity of muscle stem cells. He is currently an associate professor at the Faculty of Laboratory Medicine in the Third Military Medical University. His research interests include exploring the effect of microenvironment on the stem cell, mainly using skeletal muscle and hemopoietic system as the model, and bioinformatics.

References

1. Schiaffino, S.; Patridge, T., editors. Advances in muscle research in muscle research. Vol. 3. Springer; 2008. Skeletal muscle repair and regeneration..

2. Braz J, Bueno O, Liang Q, Wilkins B, Dai Y, Parsons S, et al. Targeted inhibition of p38 MAPK promotes hypertrophic cardiomyopathy through upregulation of calcineurin-NFAT signaling. J Clin Invest. 2003; 111(10):1475–86. [PubMed: 12750397]

3. Wang Y, Huang S, Sah V, Ross J Jr, Brown J, Han J, et al. Cardiac muscle cell hypertrophy and apoptosis induced by distinct members of the p38 mitogen-activated protein kinase family. J Biol Chem. 1998; 273(4):2161–8. [PubMed: 9442057]

4. O'Cochlain D, Perez-Terzic C, Reyes S, Kane G, Behfar A, Hodgson D, et al. Transgenic overexpression of human DMPK accumulates into hypertrophic cardiomyopathy and myotonic myopathy and hypotension traits of myotonic dystrophy. Hum Mol Genet. 2004; 13(20):2505–18. [PubMed: 15317754]

5. Sasaoka T, Imamura M, Araishi K, Noguchi S, Mizuno Y, Takagoshi N, et al. Pathological analysis of muscle hypertrophy and degeneration in muscular dystrophy in gamma-sarcoglycan-deficient mice. Neuromuscul Disord. 2003; 13(3):193–206. [PubMed: 12609501]

6. Gilhuis H, Zophel O, Lammens M, Zwarts M. Congenital monomelic muscular hypertrophy of the upper extremity. Neuromuscul Disord. 2009; 19(10):714–7. [PubMed: 19751976]

7. Li M, Dalakas M. Expression of human IAP-like protein in skeletal muscle: a possible explanation for the rare incidence of muscle fiber apoptosis in T-cell mediated inflammatory myopathies. J Neuroimmunol. 2000; 106(1–2):1–5. [PubMed: 10814776]

8. Phillips T, Leeuwenburgh C. Muscle fiber specific apoptosis and TNF-alpha signaling in sarcopenia are attenuated by life-long calorie restriction. FASEB J. 2005; 19(6):668–70. [PubMed: 15665035]

9. Tidball J. Inflammatory processes in muscle injury and repair. Am J Physiol Regul Integr Comp Physiol. 2005; 288(2):R345–53. [PubMed: 15637171]

10. Berendse M, Grounds MM, Lloyd C. Myoblast structure affects subsequent skeletal myotube morphology and sarcomere assembly. Exp Cell Res. 2003; 291(2):435–50. [PubMed: 14644165]

11. Formigli L, Meacci LE, Zecchi-Orlandini S, Orlandini G. Cytoskeletal reorganization in skeletal muscle differentiation: from cell morphology to gene expression. Eur J Histochem. 2007; 51(Suppl. 1):21–8. [PubMed: 17703590]

12. Emery A. The muscular dystrophies. Lancet. 2002; 359(9307):687–95. [PubMed: 11879882]

13. Bogdanovich S, Perkins K, Krag T, Khurana T. Therapeutics for Duchenne muscular dystrophy: current approaches and future directions. J Mol Med. 2004; 82(2):102–15. [PubMed: 14673527]

14. Blau H. Cell therapies for muscular dystrophy. N Engl J Med. 2008; 359(13):1403–5. [PubMed: 18815403]

15. Contestabile A. Amyotrophic lateral sclerosis: from research to therapeutic attempts and therapeutic perspectives. Curr Med Chem. 2011; 18(36):5655–65. [PubMed: 22172070]

16. Angelini C. Diagnosis and management of autoimmune myasthenia gravis. Clin Drug Investig. 2011; 31(1):1–14.

17. Mercuri E, Muntoni F. Muscular dystrophy: new challenges and review of the current clinical trials. Curr Opin Pediatr. 2013; 25(6):701–7. [PubMed: 24240289]

18. Flanigan KM. The muscular dystrophies. Semin Neurol. 2012; 32(3):255–63. [PubMed: 23117950]

19. Yang Z, Wang Y, Li Y, Liu Q, Zeng Q, Xu X. Options for tracking GFP-labeled transplanted myoblasts using in vivo fluorescence imaging: implications for tracking stem cell fate. BMC Biotechnol. 2014; 14:55. [PubMed: 24919771]

20. Xu X, Yang Z, Liu Q, Wang Y. In vivo fluorescence imaging of muscle cell regeneration by transplanted EGFP-labeled myoblasts. Mol Ther. 2010; 18(4):835–42. [PubMed: 20125125]

21. Kasper CE, Xun L. Cytoplasm-to-myonucleus ratios in plantaris and soleus muscle fibres following hindlimb suspension. J Muscle Res Cell Motil. 1996; 17(5):603–10. [PubMed: 8906626]

22. Tseng BS, Kasper CE, Edgerton VR. Cytoplasm-to-myonucleus ratios and succinate dehydrogenase activities in adult rat slow and fast muscle fibers. Cell Tissue Res. 1994; 275(1): 39–49. [PubMed: 8118846]

23. Rando T, Blau HM. Primary mouse myoblast purification, characterization, and transplantation for cell-mediated gene therapy. J Cell Biol. 1994; 125(6):1275–87. [PubMed: 8207057]

24. Gonzalez, RC.; Woods, RE. Digital image processing. 2nd ed.. Prentice Hall; Upper Saddle River: 2002.

25. Palágyi K, Kuba A. A 3D 6-subiteration thinning algorithm for extracting medial lines. Pattern Recognit Lett. 1998; 19(7):613–27.

26. da F Costa, L.; Cesar, RM. Shape classification and analysis: theory and practice. 2nd ed.. CRC Press; Boca Raton, FL: 2009.

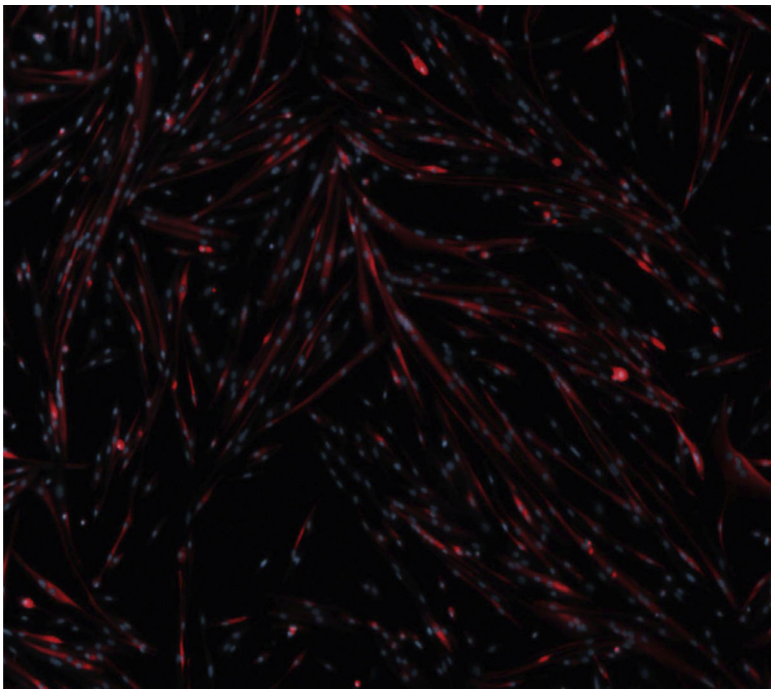

Fig. 1.

An original image showing both cytoplasm and nuclei of harvested TA muscle from a mouse model of muscular dystrophy. We can observe that cytoplasm generally has an elongated ellipsoidal shape. Due to the presence of nuclei and other factors in imaging, cytoplasm has an uneven signal intensity, making them a challenge for automatic detection.

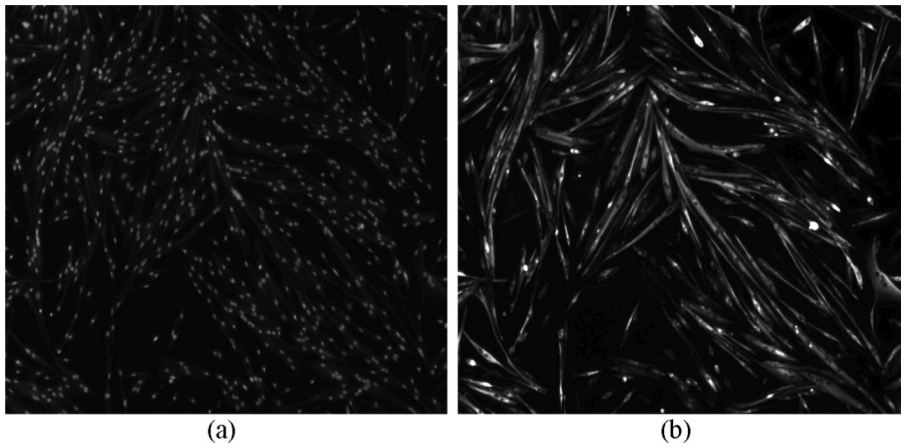

Fig. 2.

(a) The DAPI channel of Fig. 1 showing nuclei, from which we can observe some residual signals from the MHC channel. (b) The MHC channel of cytoplasm, from which we can observe that as nuclei are not stained by MHC they constitute dark holes in cytoplasm.

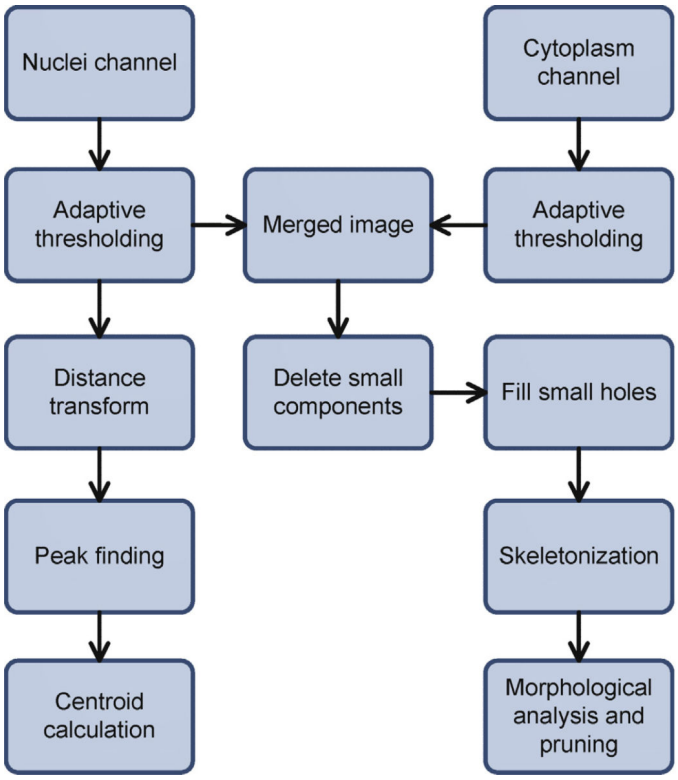

Fig. 3.

The proposed image processing pipeline. The branch to the left is for nuclei channel processing. The branch to the right is for cytoplasm channel processing.

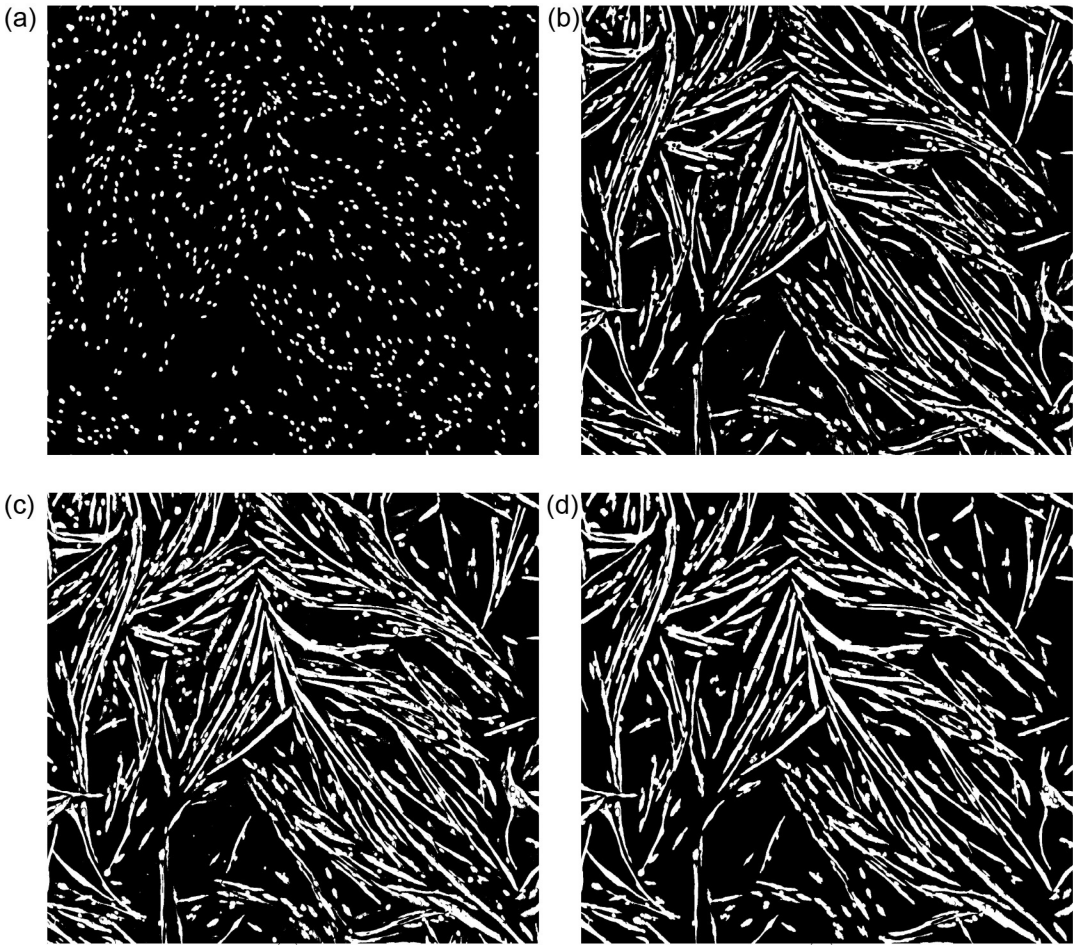

Fig. 4.

Processing results of Fig. 2. (a) The detected nuclei. (b) The intermediate result of detecting cytoplasm. Note that holes caused by nucleus staining and small scatters are still present in this result. (c) Holes caused by nucleus staining are filled. (d) Small scatters have been removed in the cytoplasm result.

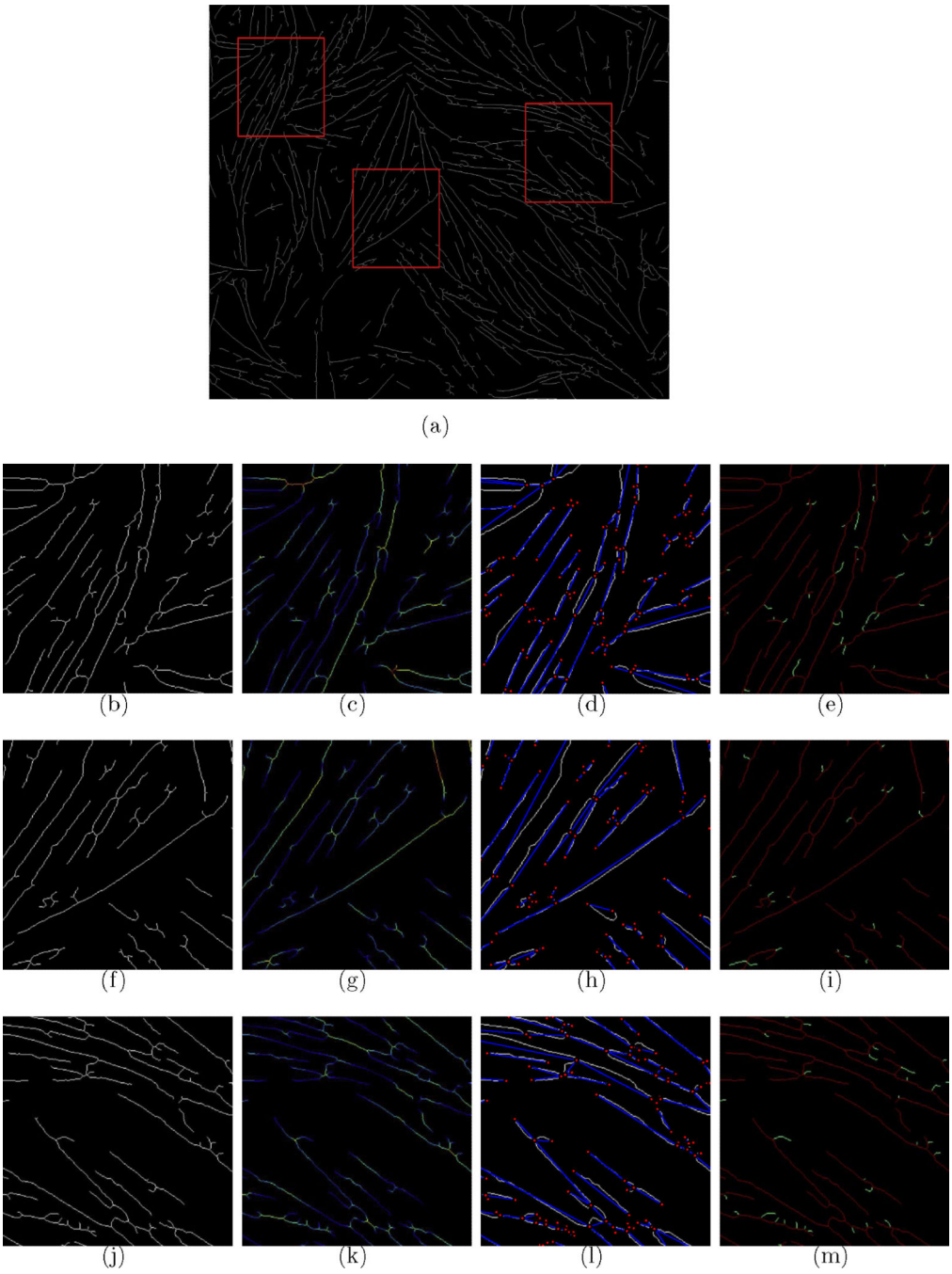

Fig. 5.

Topological representation of the cytoplasm. (a) Skeleton obtained from Fig. 4 by thinning. Three regions of interest (ROIs) are selected for detailed illustration. (b, f, and j) The three ROIs in (a). (c, g, and k) Color maps of (b, f, and j), respectively, showing the distance of the skeleton to the borders of cytoplasm, i.e., half the width of the cytoplasm at each point. (d, h, and l) Network reconstructed from the skeleton of (b, f, and j), respectively. (e, i, and m) Small removed branches are shown in green, the final skeletons are shown in red.

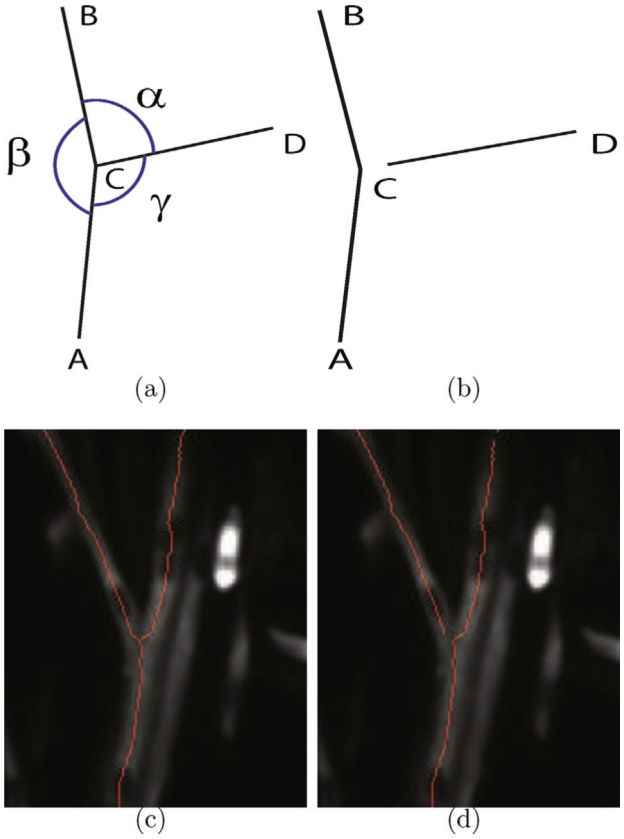

Fig. 6.

Procedure to separate overlapping or adjacent cytoplasm. (a) We first calculate the angles formed at a bifurcation point. (b) We can perform an "open" operation to separate the line section that does not form an approximate straight line with the other line sections. In case, line section $\overline{DC}$ is determined to be the skeleton of a separate cytoplasm while line section $\overline{ACB}$ is considered as the skeleton of the same cytoplasm. (c) The corresponding example of (a). (d) The corresponding result of (c) after cytoplasm separation.

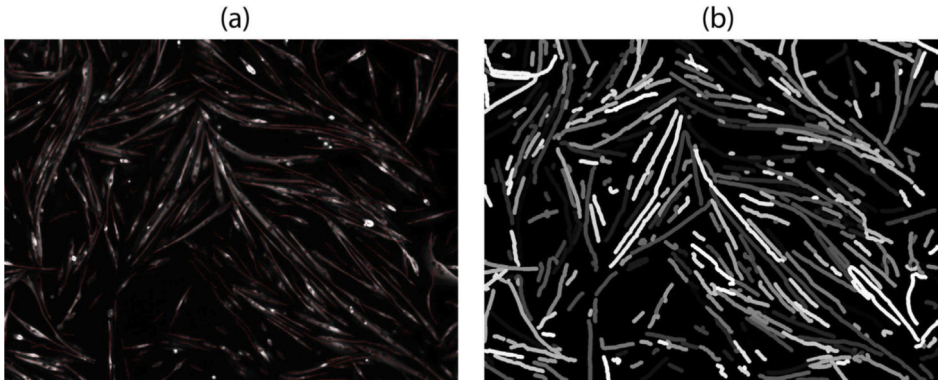

Fig. 7.

(a) Final skeleton superimposed to the original image. (b) The detected segments are expanded to represent the original fibers.

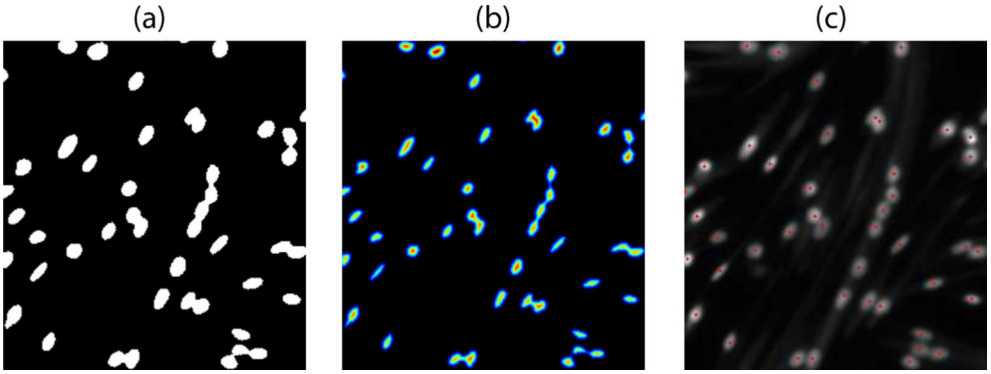

Fig. 8.

(a) Example of a binarized nuclei image, from which we note there are adjacent nuclei. (b) Distance transform of the binary image. (c) Identified nuclei marked in red overlaid into the original image. Note that the adjacent nuclei are well separated.

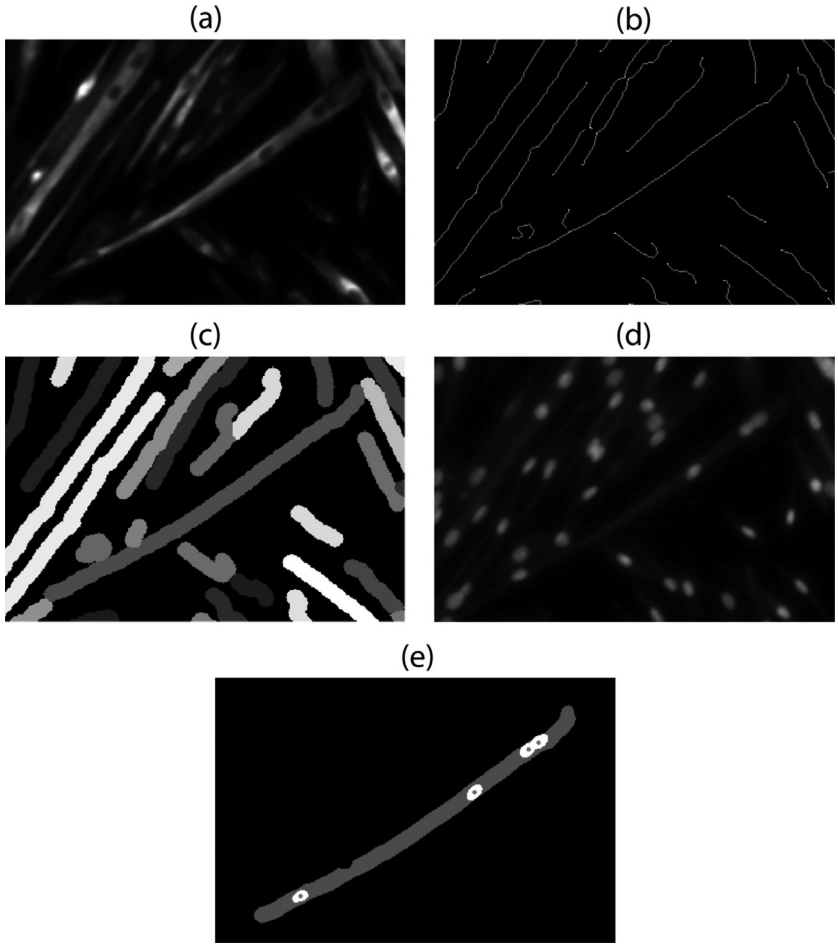

Fig. 9.

Illustration of the main steps of the procedure proposed in this paper for a single fiber. (a) Original cytoplasm image, zoomed in a single fiber (shown at the center). (b) Skeletons of (a). (c) Dilated skeletons representing an idealization of the original cytoplasm. (d) Zoomed in area of the original nuclei image. (e) Final result showing the fiber with its nuclei.

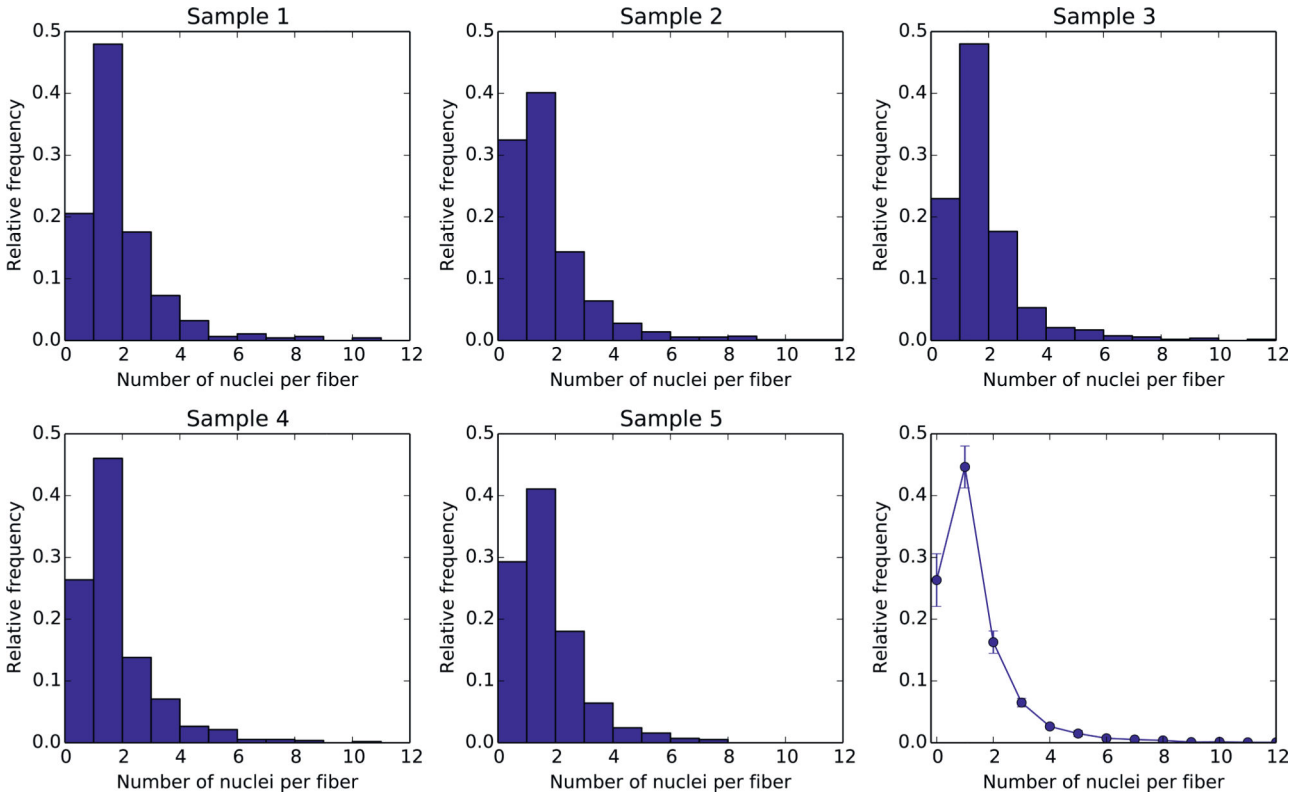

Fig. 10.

Histograms for the number of nuclei per cytoplasm. Each bar plot corresponds to a sample. The line plot is the average of all histograms into the same axes.

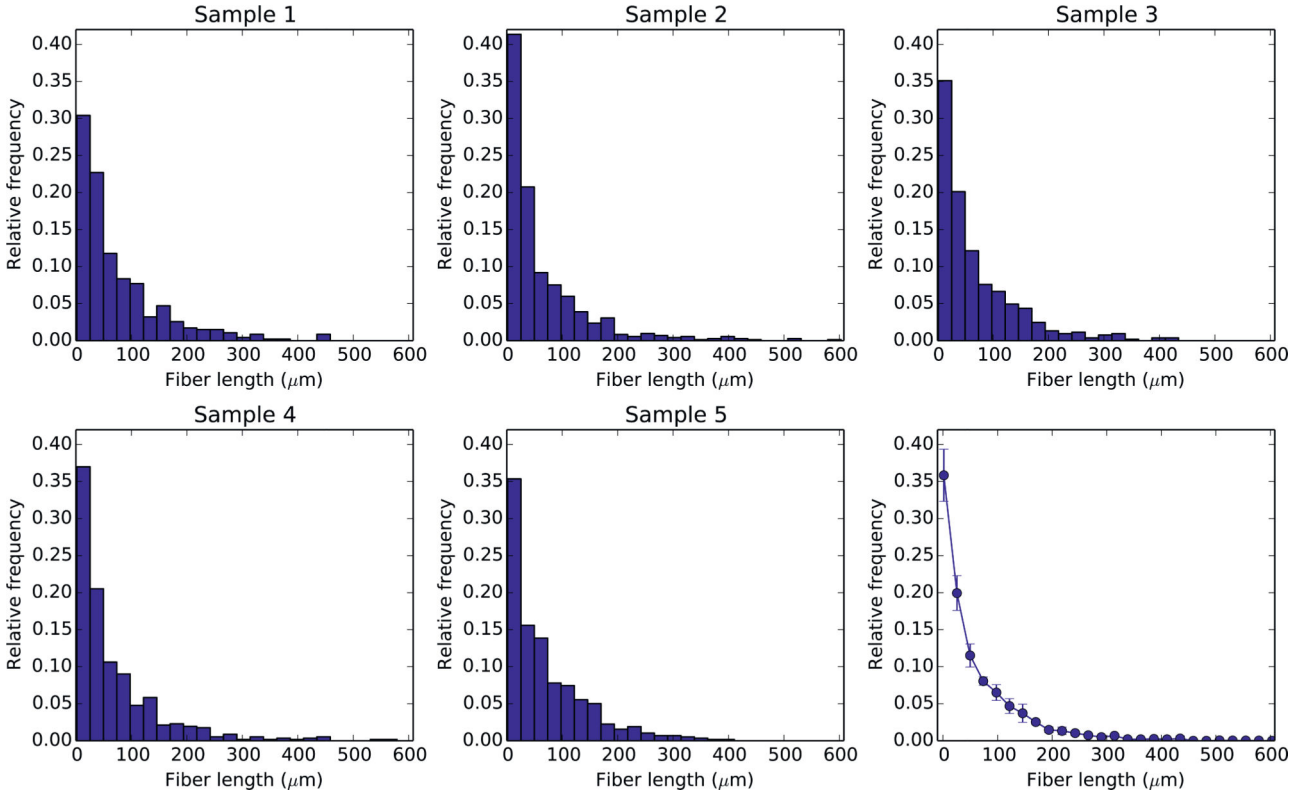

Fig. 11.

Fiber lengths of five muscular tissue specimens. The last picture plots the average fiber length with its standard deviation.

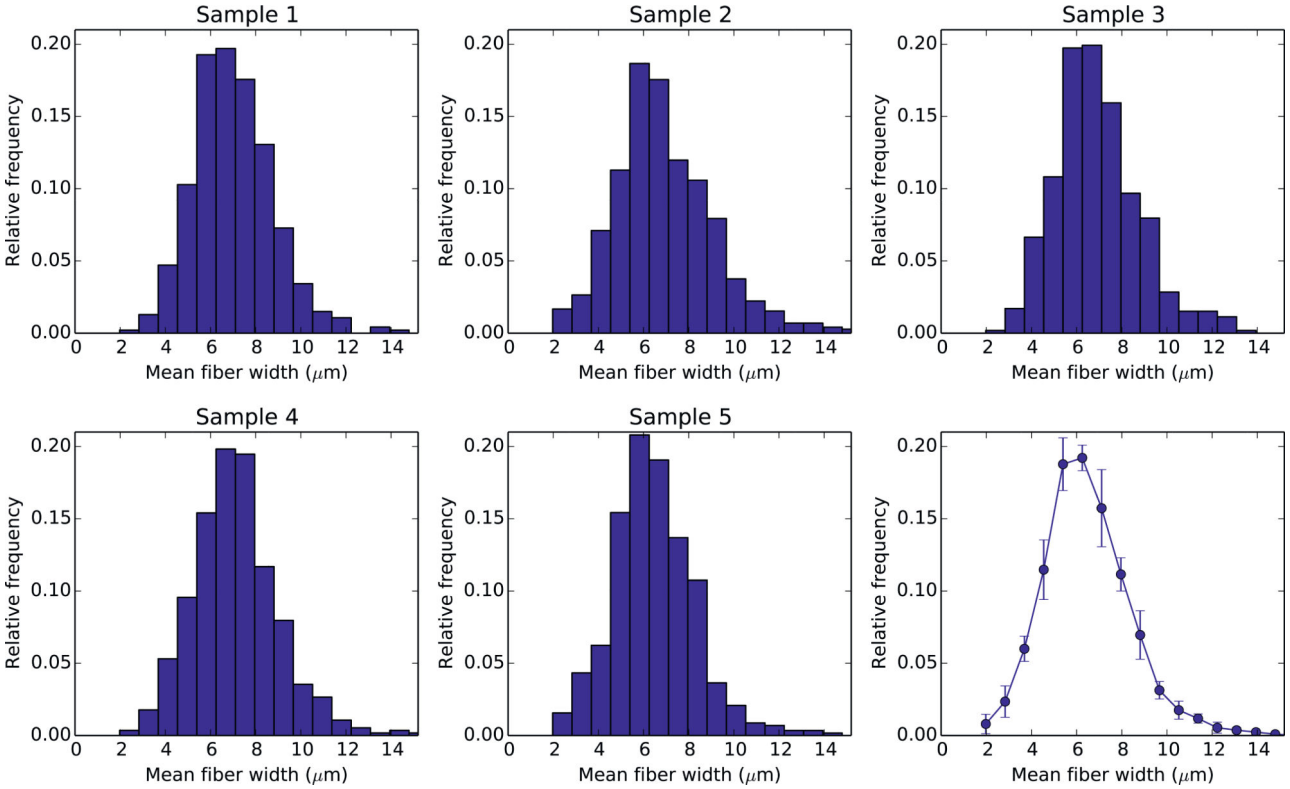

Fig. 12.
Mean fiber width.

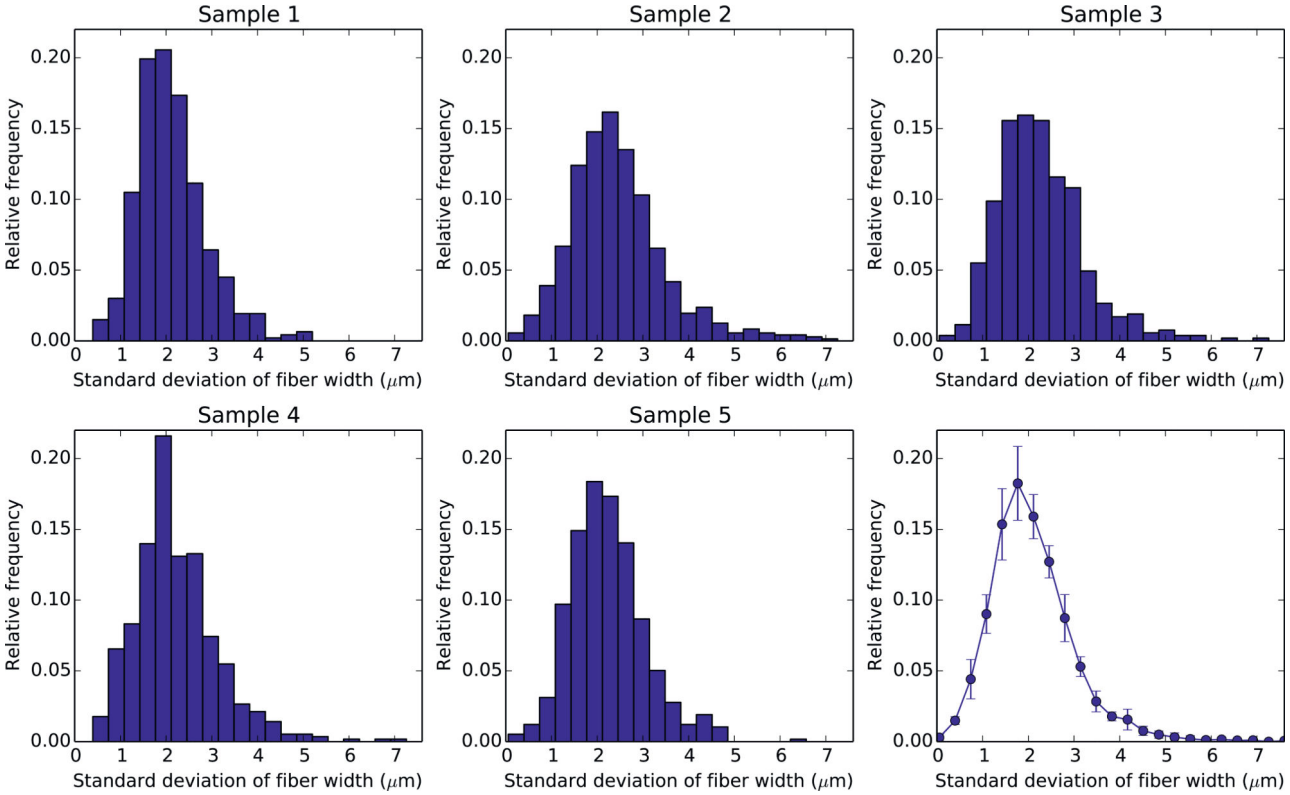

Fig. 13.
Deviation of fiber width.

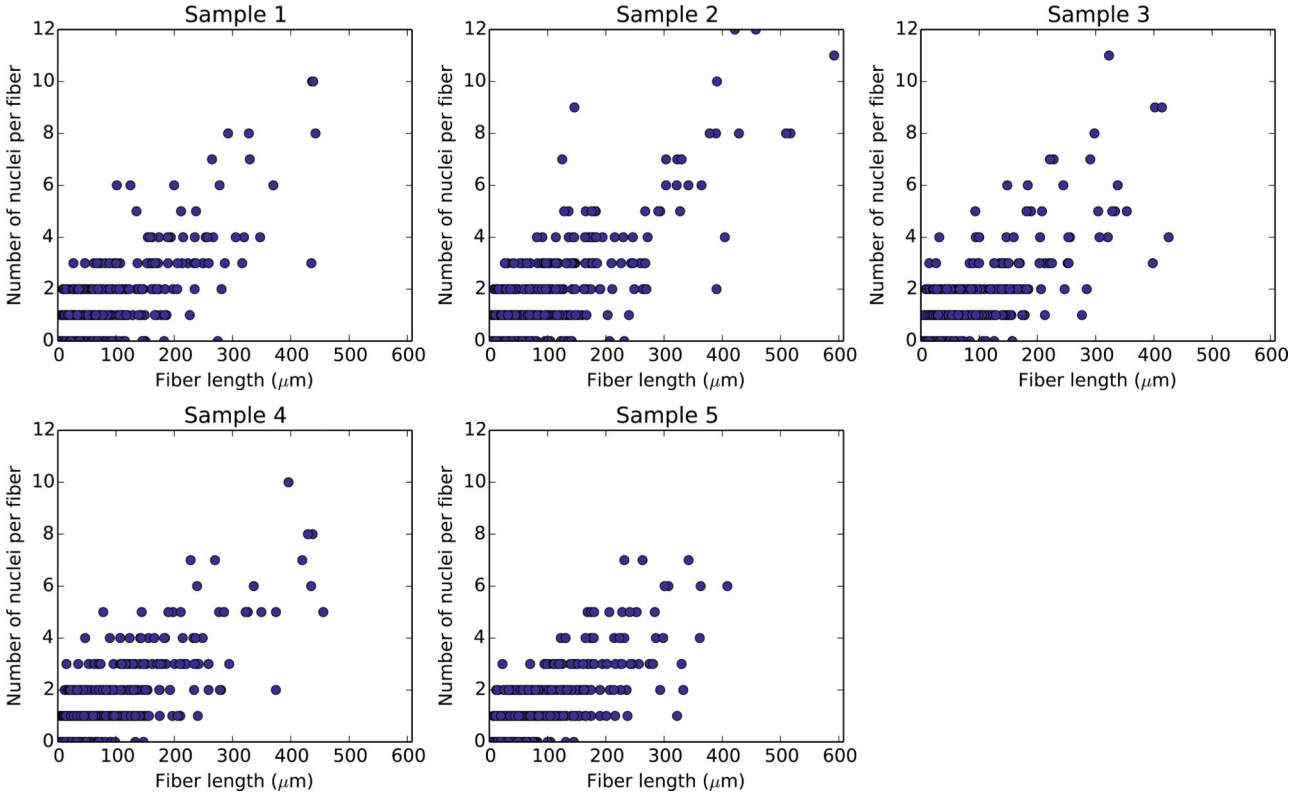

Fig. 14.
Number of nuclei per fiber length.

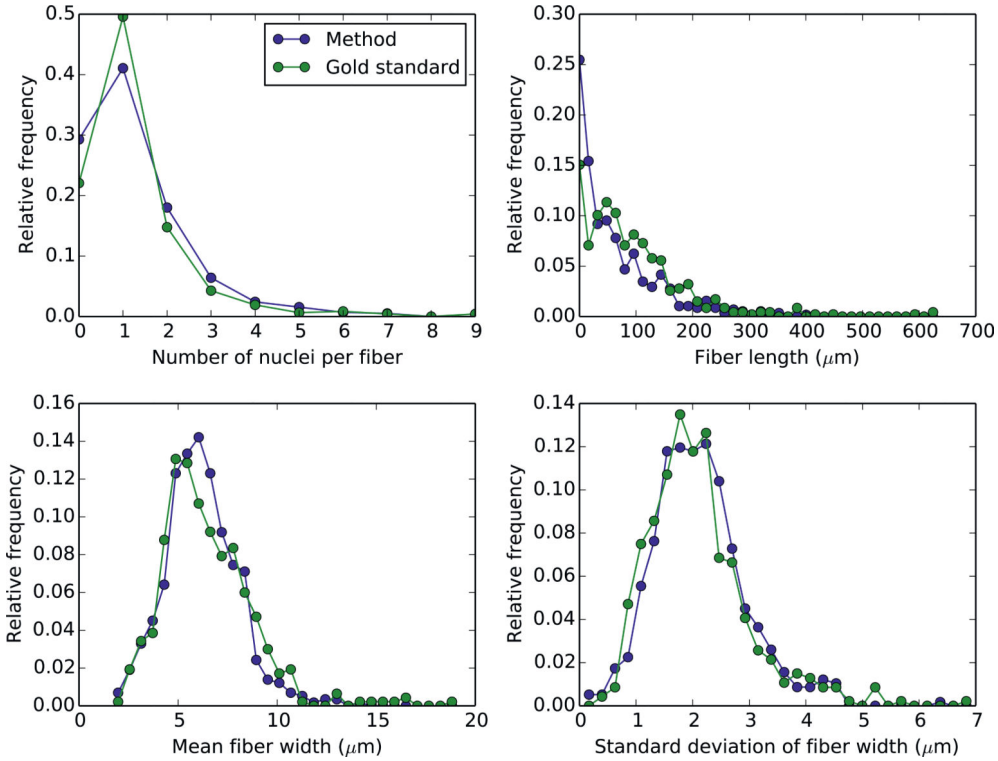

Fig. 15.

Comparison between the gold standard and our method for the automatic segmentation of muscle fibers. All four automatically measured quantities are close to the ground truth. The results of the manual segmentation can be found in Fig. S1 of the supplementary material.

Table 1

Values obtained for five muscle fiber images and the gold standard. The gold standard is the manual segmentation of sample number 5.

Sample	Nuclei density (μm^{-2})	Fiber density (μm^{-2})	Fraction of fiber area	Nuclei per fiber area (μm^{-2})	Total fiber length (μm)
1	0.00077	0.00042	0.23	0.0034	35,767
2	0.00101	0.00065	0.30	0.0034	46,089
3	0.00079	0.00048	0.24	0.0033	37,040
4	0.00086	0.00051	0.26	0.0033	39,467
5	0.00077	0.00052	0.24	0.0032	40,994
Gold standard of sample 5	0.00083	0.00046	0.29	0.0029	42,292